Journal of Fluids and Structures (2000) **14,** 257–273
doi: 10.1006/jfls. 1999.0266, available online at http://www.idealibrary.com on IDEAL®

ON MARINE RISER RESPONSES IN TIME- AND DEPTH-DEPENDENT FLOWS

G. K. Furnes

Norsk Hydro E&P Research Centre, Sandsliveien 90 N-5020 Bergen, Norway

(Received 2 November 1998, and in final form 6 October 1999)

A mathematical formulation for solving the beam equation is developed and applied to describe marine riser motions due to current forces. The method is sufficiently flexible to consider arbitrary currents that vary continuously with depth and time. The relative motions between the riser and the free currents are converted to forces using a simplified formulation, leading to a linear damping and a current drag that is proportional to the square of the current speed. The drag coefficient can vary with time and is used to simulate vortex-induced vibrations where the Strouhal number is permitted to vary along the riser. The expansions for riser displacements are given in terms of time-varying coefficients together with axial varying functions (eigenfunctions). The evolution of the coefficients are determined through a numerical time-integration procedure, while the functions are computed once through an eigenvalue problem. A continuous axial variation of the displacements and bending moments with time are computed using this method. The method is applied to two physical test-cases that have been carried out to study vortex-induced vibrations. The tests employed risers that were approximately 11 and 90 m long. Comparisons between simulated and measured displacements and bending moments revealed a good correspondence between modelled and measured data. This was achieved without tuning of the drag and damping coefficients. The energy-conserving properties of the model are also demonstrated by forcing the model by an impulse load.

1. INTRODUCTION

As offshore oil-gas exploration and production are moving towards deeper water, there is increasing attention on drag forces caused by ocean currents. A significant contribution to the total drag may be due to the risers. The drag forces may lead to considerable static displacements, and under certain conditions, to vortex-induced vibrations (VIV) and possible fatigue damage. The design of risers therefore requires attention to fatigue life. There is a vast literature on VIV studies, mostly for cylindrical structures, and a review article was published by King (1977). A comprehensive and well-written presentation of the vortex-shedding phenomenon and the problem of predicting VIV of slender marine structures can be found in Halse (1997).

Considerable effort has been made in recent years to develop computer codes capable of computing riser responses. This development has followed two main directions as follows.

1. Simplified engineering models where the fluid–structure interactions are considerably simplified. One such program is known as SHEAR7, developed at MIT and widely used in the industry (Vandiver & Li 1994). The advantages of this type of model are simplicity and cost efficiency with respect to computational resources. One of the disadvantages is the introduction of the added mass (entrainment mass) formulation that introduces an uncertainty into the calculations. The model presented in this paper belongs to this category.
2. Computational fluid dynamics (CFD) models coupled with a structure model, usually denoted by FSI model (Fluid structure interaction). With these models, it is possible to give

a realistic resolution of the flowfield around a moving boundary and hence opens the opportunity to have a more correct forcing (pressure and viscous) on the riser. One such code is known as Nektar, developed at Brown University [see, e.g., Newman & Karniadakis (1997)].

Nektar has unique capabilities which allow a direct numerical simulation (DNS) of turbulent flow past freely vibrating cables and beams. It uses two different formulations of the moving domain: a boundary-fitted-coordinate system, and an arbitrary-Lagrangian–Eulerian formulation. It also uses spectral methods on an unstructured grid, greatly reducing the required computational effort. FSI models applied to long and slim bodies like a riser will require enormous computer power that is not generally available today.

The model presented in this paper is based on a spectral method solution of the beam equation where the current forcing is allowed to vary in time and over depth. A forcing frequency is prescribed through the drag (or lift) coefficients and is based on the Strouhal number. Simulations carried out with Nektar indicate that the Strouhal number has a significant variation from node to antinode (Karniadakis, private communication), and in this work the Strouhal number is allowed to vary along the riser. Numerical results are computed and presented for the transverse vibrations and validated against measurements.

2. MODEL FORMULATION

The equation describing the transverse motion of a beam will now be utilized to examine the dynamics of flow-induced riser deflections and bending moments. Suppose that a cylindrical riser whose ends are at $x = 0$ and $x = L$ is coincident with the x-axis at time $t = 0$.

Then, at time $t > 0$, a force is applied transversly on the riser, leading to a transverse deflection $y(x, t)$ which satisfies the differential equation

$$m\frac{\partial^2 y}{\partial t^2} + \frac{\partial^2}{\partial x^2}\left(EI\frac{\partial^2 y}{\partial x^2}\right) + \frac{\partial}{\partial x}\left(T\frac{\partial y}{\partial x}\right) = F - F_d, \quad 0 < x < L, \quad t > 0. \tag{1}$$

In this equation, E is Young's modulus of elasticity, I the second moment of area, T the axial tension ($T < 0$), F the hydrodynamic forcing, F_d the hydrodynamic damping including structure damping, and m the structure mass per unit length including added mass. The quantity EI, the flexural rigidity of the riser, is assumed to be constant, and $EI(\partial^2 y/\partial x^2)$ is the bending moment. The axial tension T is generally varying with x but will here be considered as constant. This can be justified for application to the risers described in the subsequent paragraphs.

A linear damping force formulation will be employed in this study and is given by

$$F_d = R\frac{\partial y}{\partial t},$$

where R is a prescribed constant. Equation (1) can then be written as

$$\frac{\partial^2 y}{\partial t^2} + \frac{R}{m}\frac{\partial y}{\partial t} + \frac{EI}{m}\frac{\partial^4 y}{\partial x^4} + \frac{T}{m}\frac{\partial^2 y}{\partial x^2} = \frac{F}{m}. \tag{2}$$

A scaling of the x-coordinate $x = \xi L$ is introduced, and then for any particular location ξ let $\phi_n(\xi)$ be an arbitrary differentiable function defined within the range $0 \le \xi \le 1$. Multiplication of the scaled beam equation (2) by $\phi_n(\xi)$, and integration with respect to ξ, from $\xi = 0$ to $\xi = 1$, gives

$$\frac{\mathrm{d}^2\hat{Y}_n}{\mathrm{d}t^2} + a\frac{\mathrm{d}\hat{Y}_n}{\mathrm{d}t} + b\int_0^1 \frac{\partial^4 y}{\partial \xi^4}\phi_n\,\mathrm{d}\xi + p\int_0^1 \frac{\partial^2 y}{\partial \xi^2}\phi_n\,\mathrm{d}\xi = \frac{1}{m}\int_0^1 F\phi_n\,\mathrm{d}\xi. \tag{3}$$

In this equation

$$\hat{Y}_n = \int_0^1 y\phi_n \, d\xi \tag{4}$$

and

$$a = \frac{R}{m}, \quad b = \frac{EI}{mL^4}, \quad p = \frac{T}{mL^2}.$$

By integrating the third term of equation (3) by parts four times, and similarly twice for the fourth term, equation (3) is converted to

$$\frac{d^2\hat{Y}_n}{dt^2} + a\frac{d\hat{Y}_n}{dt} + b\int_0^1 y\frac{d^4\phi_n}{d\xi^4}\,d\xi + p\int_0^1 y\frac{d^2\phi_n}{d\xi^2}\,d\xi = \frac{1}{m}\int_0^1 F\phi_n\,d\xi + B_n. \tag{5}$$

B_n contains the boundary conditions that need to be prescribed at the riser end-points $\xi = 0$ and 1. This term is given by

$$B_n = b\left[-\frac{\partial^3 y}{\partial\xi^3}\phi_n + \frac{\partial^2 y}{\partial\xi^2}\frac{d\phi_n}{d\xi} - \frac{\partial y}{\partial\xi}\frac{d^2\phi_n}{d\xi^2} + y\frac{d^3\phi_n}{d\xi^3}\right]_0^1 + p\left[-\frac{\partial y}{\partial\xi}\phi_n + y\frac{d\phi_n}{d\xi}\right]_0^1. \tag{6}$$

Taking ϕ_n to satisfy

$$\frac{d^4\phi_n}{d\xi^4} = \lambda_n^2\phi_n \tag{7}$$

the choice of boundary conditions (see Section 4) will automatically yield

$$\frac{d^2\phi_n}{d\xi^2} = -\lambda_n\phi_n. \tag{8}$$

The direct substitution of equations (7) and (8) into equation (5) gives the transformed equation of motion

$$\frac{d^2\hat{Y}_n}{dt^2} + a\frac{d\hat{Y}_n}{dt} + (b\lambda_n - p)\lambda_n\hat{Y}_n = \frac{1}{m}\int_0^1 F\phi_n\,d\xi + B_n, \tag{9}$$

where $\hat{Y}_n$ is only a function of time. With a given set of boundary conditions, equation (7) may be integrated to determine ϕ_n, λ_n. From prescribed initial conditions and a formulation of the forcing term F, the time-evolution of the integral transformation $\hat{Y}_n$ is computed from equation (9). The displacement y can then be found by inverting the integral transform given by equation (4).

3. THE INVERSE TRANSFORMATION

It is easy to show that equation (7), together with a set of homogeneous boundary conditions, leads to an eigenvalue problem with infinitely many solutions, λ_n denoting the ascending eigenvalues and ϕ_n the corresponding eigenfunctions. If the general solution of equation (2) is expressed by a series expansions in terms of the orthogonal functions ϕ_n,

$$y = \sum_{r=1}^{\infty} A_r(t)\,\phi_r(\xi), \tag{10}$$

the inverse transformation of equation (4) is straightforward. Introducing the expansion (10) into equation (4), the only contribution to the integral is for $r = n$ due to the orthogonality. The expansion coefficient A_n in equation (10) can then be expressed by

$$A_n = \frac{\hat{Y}_n}{\int_0^1 \phi_n^2 \, \mathrm{d}\xi}. \tag{11}$$

By denoting

$$\Phi_n = \frac{1}{\int_0^1 \phi_n^2 \, \mathrm{d}\xi}, \tag{12}$$

the displacement is given by

$$y = \sum_{r=1}^{\infty} \Phi_r \hat{Y}_r(t) \, \phi_r(\xi). \tag{13}$$

Having now an expression for the displacement y, which can be evaluated continuously over $0 \leq \xi \leq 1$, it is easy to find expressions for the bending moments and the tensions. The bending moment M can be computed from

$$M = EIy'' = EI \sum_{r=1}^{\infty} \Phi_r \hat{Y}_r \phi_r'', \tag{14}$$

where the prime denotes differentiation with respect to ξ. Having determined the bending moment, the corresponding stress is given by

$$\sigma = \frac{M}{I} \frac{D}{2},$$

where D is the diameter of the riser.

The change in axial tension is proportional to the relative elongation of the riser associated with the deflection y. By denoting the length of the riser at time $t > 0$ by S, the relation between S and y can be expressed by

$$\frac{\mathrm{d}S}{L\mathrm{d}\xi} = \sqrt{1 + \frac{1}{L^2} \, y'^2}. \tag{15}$$

Differentiating y in equation (13) with respect to ξ, substituting for y' in equation (15) and then integrating from $\xi = 0$ to 1, yields the following expression for S:

$$\frac{S}{L} = \int_0^1 \left[1 + \frac{1}{L^2} \left(\sum_{r=1}^{\infty} \Phi_r \hat{Y}_r \phi_r' \right)^2 \right]^{1/2} \mathrm{d}\xi. \tag{16}$$

It is evident that S/L is always greater or equal to one. The next step is to determine ϕ_n, λ_n and Φ_n.

4. EIGENFUNCTIONS AND EIGENVALUES

The general solution of equation (7) is given by

$$\phi_n = c_1 \sin(\sqrt{\lambda_n}\xi) + c_2 \cos(\sqrt{\lambda_n}\xi) + c_3 \mathrm{e}^{\sqrt{\lambda_n}\xi} + c_4 \mathrm{e}^{-\sqrt{\lambda_n}\xi}, \tag{17}$$

where c_1 to c_4 are constants to be determined from the boundary conditions.

The boundary conditions associated with the differential equation (7) depend on the manner in which the riser is supported at the end-points. The following are the most common: (i) clamped, built-in or fixed end: $y = y' = 0$; (ii) hinged or simply-supported end: $y = y'' = 0$; (iii) free end: $y'' = y''' = 0$.

Boundary condition (ii) will be employed in the present paper due to its relevance for the model validation discussed in Sections 6 and 7. The boundary conditions are hence

$$\phi_n(0) = 0, \quad \phi_n(1) = 0, \quad \phi_n''(0) = 0, \quad \phi_n''(1) = 0$$

which together with scaling or normalizing of ϕ_n lead to the following result:

$$\phi_n = \sin \sqrt{\lambda_n}\xi, \quad \sqrt{\lambda_n} = (n-1)\pi, \tag{18}$$

where $n = 1, 2, \ldots, \infty$. It is evident that the solutions of equation (7) given by equation (18) satisfy equation (8) as well.

Introducing equation (18) into equation (12) leads to

$$\Phi_n = 2, \quad n = 1, 2, \ldots, \infty.$$

Finally, introducing the boundary conditions into equation (6) yields

$$B_n = 0, \quad n = 1, 2, \ldots, \infty.$$

5. HYDRODYNAMIC FORCING

Before the solution of equation (9) for $\hat{Y}_n$ can be obtained, it is necessary to describe the hydrodynamic forcing represented by F. Generally, F represents the total pressure and viscous forces acting per unit length of the riser. A model formulation based on the Navier–Stokes equations could be used for this purpose. As the riser boundaries are moving in time and the flow field is three-dimensional and time-varying, this will lead to a tremendous computational task. A simpler formulation will therefore be applied in this paper, where F is specified by

$$F = \tfrac{1}{2}\rho C_d D|U|U. \tag{19}$$

Here $U(\xi, t)$ is the current speed, D is the riser diameter, ρ is the density of the surrounding liquid and C_d is the nondimensional drag (or lift) coefficient. The drag/lift coefficient will be expressed by

$$C_d = C_0 + C_1 \sin(2\pi f t), \tag{20}$$

where f is the forcing frequency that must be determined. When the riser motions are small and outside the "lock-in" mode, it is natural to relate f to the vortex-shedding frequency f_s, determined from

$$f_s = \frac{\mathrm{St}\, U}{D}, \tag{21}$$

where St is the Strouhal number. The frequency of the lift and the drag force may then be given by $f = f_s$ and $f = 2f_s$, respectively. In the "lock-in" mode the vortex shedding is apparently controlled by the riser motion itself and may be deduced from some of the natural frequencies of the participating modes of the riser system.

To resolve the vertical structure of the currents, the axial coordinate of the riser is divided into M intervals bounded by the coordinates $\xi_0, \xi_1, \ldots, \xi_M$, where ξ_0 is at $\xi = 0$ and ξ_M is at

$\xi = 1$. The velocity profile will be approximated by layers of piecewice linear functions. For the interval $\xi_k < \xi < \xi_{k+1}$ the velocity is given by

$$U(\xi, t) = b_k(t)\,\xi + c_k(t), \tag{22}$$

where

$$b_k = \frac{U_{k+1} - U_k}{\xi_{k+1} - \xi_k}, \quad c_k = \frac{U_k\xi_{k+1} - U_{k+1}\xi_k}{\xi_{k+1} - \xi_k}.$$

The depth mean current over the interval $L_k = \xi_{k+1} - \xi_k$ is then

$$\bar{U}_k \frac{1}{L_k} \int_{\xi_k}^{\xi_{k+1}} (b_k\xi + c_k)\,\mathrm{d}\xi = \frac{b_k}{2}\,(\xi_{k+1} + \xi_k) + c_k. \tag{23}$$

The frequency f and drag coefficient C_d will be considered as piecewise constant over the considered interval and denoted by f_k and $C_d^{(k)}$, respectively. Hence, in view of equations (20) and (21),

$$C_d^{(k)} = C_0^{(k)} + C_1^{(k)} \sin(2\pi f_k t),$$

where

$$f_k = \frac{\mathrm{St}^{(k)}\,\bar{U}_k}{D}.$$

The hydrodynamic forcing given by equation (19), over the interval $\xi_k < \xi < \xi_{k+1}$ can then be written as

$$F_k = \delta\,\tfrac{1}{2}\,\rho C_d^{(k)} D(b_k\xi + c_k)^2,$$

where $\delta = 1$ for $U \geq 0$ and $\delta = -1$ for $U < 0$. The forcing term in equation (9) can now be expressed by

$$\frac{1}{m}\int_0^1 F\phi_n\,\mathrm{d}\xi = \frac{1}{m}\sum_{k=1}^{M}\int_{\xi_{k-1}}^{\xi_k} F_k\phi_n\,\mathrm{d}\xi = \delta\,\frac{\rho D}{2m}\sum_{k=1}^{M} C_d^{(k)}\int_{\xi_{k-1}}^{\xi_k} (b_k\xi + c_k)^2\,\sin(\sqrt{\lambda n}\xi)\,\mathrm{d}\xi, \tag{24}$$

which can be integrated exactly.

The response of a cylindrical riser to external forcing is critically dependent upon the relationship between the forcing frequencies and the frequencies of the free vibrations (natural frequencies) of the system. It has been demonstrated experimentally [for a review of vortex shedding research, see King (1977)] that, initially, as the fluid velocity is increased from zero, the cylinder is stationary and the vortex shedding frequency follows the "Strouhal relation". However, as the lower natural frequency is approached the cylinder leaves the Strouhal frequency and begins to oscillate in its natural frequency. Increasing the velocity further, it will remain "locked" to the natural frequency over a wide velocity range and then, at a certain velocity, it will jump to the next natural frequency or return to follow the Strouhal frequency.

A complete description of the processes behind the frequency responses to changing flow does not exist so far. The method used in this paper is outlined in the following sections.

The dispersion relation for free waves along the riser can easily be deduced from equation (2) by neglecting the forcing ($F = 0$) and damping ($R = 0$). Hence,

$$f = \frac{k}{2\pi}\sqrt{\frac{T}{m}}\left(1 + \frac{EI}{T}\,k^2\right)^{1/2}, \tag{25}$$

where k is the wavenumber. For "standing waves" the wavelength Λ appears as a fraction of the riser length L,

$$\Lambda = \frac{2L}{n},$$

where n is one less than the number of nodes along the riser. The "half-wave" oscillation appears for $n = 1$ (first mode). Introducing for $k = 2\pi/\Lambda$ in equation (25) gives the discrete natural frequencies

$$f_n = \frac{n}{2L}\sqrt{\frac{T}{m}}\left(1 + \frac{EI}{T}\frac{\pi^2}{L^2}n^2\right)^{1/2}. \tag{26}$$

For a riser in which the flexural rigidity $EI \ll TL^2$, the natural frequencies of the lowest modes are determined by

$$f_n \approx \frac{n}{2L}\sqrt{\frac{T}{m}}.$$

However, as the number of modes increases, the effects of the rigidity become more and more important.

In summary, having assumed that the dynamics of cylindrical marine risers can be described by the beam equation (1), a method has been presented to solve this equation by expanding the displacement in terms of eigenfunctions through the axial direction. Coefficients of these expansions vary in time and are determined from a numerical time-stepping procedure. In this way, the transverse displacement and bending moments can be computed at any point along the riser as time advances. The hydrodynamical forcing of the riser is assumed to be proportional to the square of the flow velocity, where the vertical flow structure is approximated by piecewise linear functions. Using this method, it is possible to resolve any observed current profile, including time-dependent flow problems.

6. VALIDATION AGAINST "ROTATING RIG" DATA

Model tests have been performed with a riser in a rotating rig (Mo & Lie 1997). The diameter of the riser was 0·02 m and the total length between the pinned ends was 11·48 m. The upper part of the riser could be placed in three different positions. In this way the effect of shear flow could be tested. In all the tests, accelerations transverse to the current were measured at nine vertical positions. These time-series were integrated twice to give the displacement; for details see Mo & Lie (1997). The riser was designed for neutral buoyancy and hence the assumption of constant axial tension T should be justified.

The simulation model decribed in previous sections was set up for a test-case with uniform current profile of 0·51 m/s (Mo & Lie 1997, test 5004). The pretensioning for this test was $T = -713$ N. A constant drag coefficient of $C_0^{(k)} = 0$ and $C_1^{(k)} = 1{\cdot}0$ was applied at all depths, except for the upper 1·7 m of the riser, which was above the water surface (in air). Over this section of the riser the drag coefficient was reduced in correspondence with the difference of density between air and water. Model quantities which are not provided in Mo & Lie (1997) are the damping coefficient R and the added mass coefficient C_a. In the following calculations their values are $R = 1{\cdot}5\ \mathrm{kg\,m^{-1}\,s^{-1}}$ and $C_a = 1{\cdot}0$. The added mass contribution to m is given by the second term in

$$m = m_s + \frac{\pi}{4} C_a \rho D^2,$$

where m_s is the given structure mass per unit length. The density for water was taken as 1000 kg/m^3 and for air as 1·3 kg/m^3.

The model was started from a state of rest at time $t = 0$ and integrated forward in time in steps of $\Delta T = 0{\cdot}02$ s. The Strouhal number was prescribed at 10 spatial intervals covering a range of values from 0·15 to 0·22. After 1000 iterations (20 s), the standard deviation (STD) of the transverse deflections was calculated at a number of depths. This was done after a test of convergence of the expansion given by equation (13). The series was truncated after 50 terms, where the truncation error was far below the prescribed level.

The STD profile of the displacements are plotted in Figure 1 together with corresponding values recovered from the rotating rig experiment. It is evident from Figure 1 that the computed deflections are dominated by the third mode, which is in agreement with observations. Comparing the magnitude of the deflections, there is generally good agreement between model and observations. However, the most pronounced discrepancy appears at the two deepest measuring gauges. A reasonable explanation of this is not easy to give. Intuitively, one should expect a symmetric distribution of the STD with respect to the mid-point of the riser, if the riser was completely submerged in the water and the tension uniform. Although the simulation model to some extent incorporates effects of the air column at the upper end of the riser, through the forcing term, a series of tests have shown that the model cannot account for this discrepancy. The possibility of measuring error cannot be ruled out.

For comparison purposes the Shear7 model (Vandiver & Li 1994) was run for the same test-case with a "standard" set of parameters. The result from this is also presented in Figure 1. It is apparent from the figure that Shear7 is also predicting the third mode as dominating, but overestimates the displacements. The reason for this has not been examined, but improvements can probably be achieved by introducing a different parameter setting.

Time series of the displacement at $\xi = 0{\cdot}5$ and of the relative elongation are plotted in Figures 2 and 3, respectively, together with the associated power spectral density (PSD). The elongation is computed from equation (16) and is therefore proportional to the perturbation of the top tension. From the PSD analysis it was found that the leading frequency of the displacement is 4·3 Hz, compared to 4·11 Hz in the rig test. Figure 2 indicates also a presence of energy at 1·4 Hz. Further, a band of energy is found between 0 and 0·4 Hz.

The frequencies of the free oscillation computed from equation (16) are 1·33, 2·67 and 4·02 Hz for modes 1, 2 and 3, respectively. The peak frequency (4·3 Hz) is therefore close to the frequency corresponding to the third-mode natural frequency of the riser.

Evidently, there is also some contribution from the first mode (1·3 Hz). This is a consequence of the sudden onset of the hydrodynamic forcing at $t = 0$. However, this contribution is damped out as time progress.

Due to the quadratic term in equation (16) it is expected that the relative elongation will appear at a frequency twice the frequency of the displacement, computed from equation (13). The PSD of the elongation shows that the dominant contributions are at 0·2 and 8·6 Hz. The elongation at the highest frequency (8·6 Hz) is consequently induced by the third-mode displacement. It is interesting to observe that this is not the peak frequency of the elongation that appears at 0·2 Hz.

The subsequent comparison was carried out for a shear flow situation in which the current speed at the surface was 0·27 and 0·51 m/s at the bed. The pretensioning for this test (Mo & Lie 1997, test 5104) was $T = -729$ N. Again, the riser model was started from rest and integrated forward over a period of 20 s using the same parameters as in the previous case. Figure 4 presents the STD profile of the displacements together with data recovered

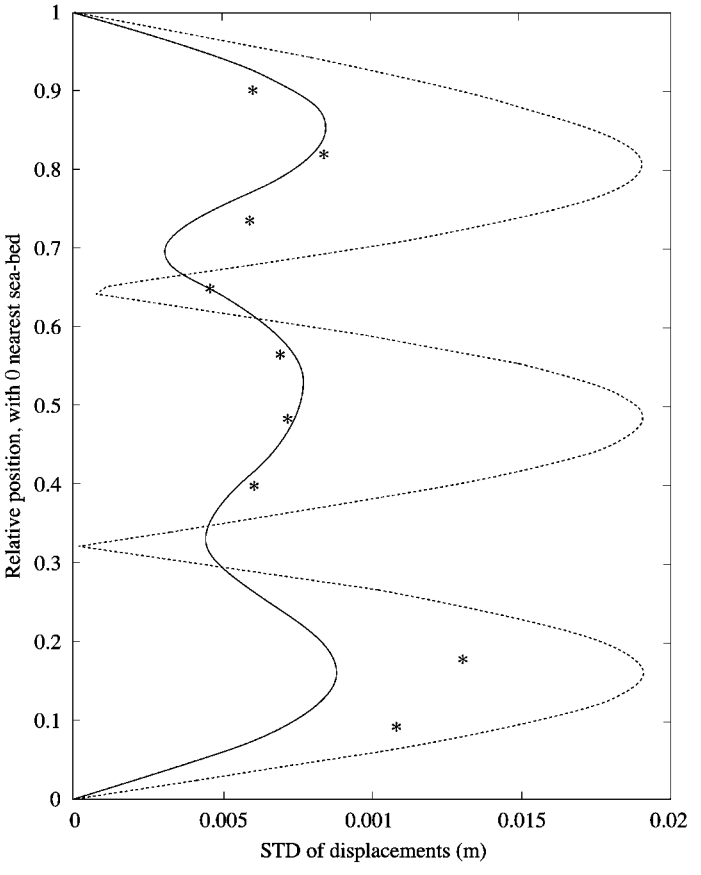

Figure 1. Comparison of STD of relative displacement (y/D) between rotating rig data (5004), present model and Shear7: —, present model; – – –, Shear7 results; ∗, rotating rig measurements.

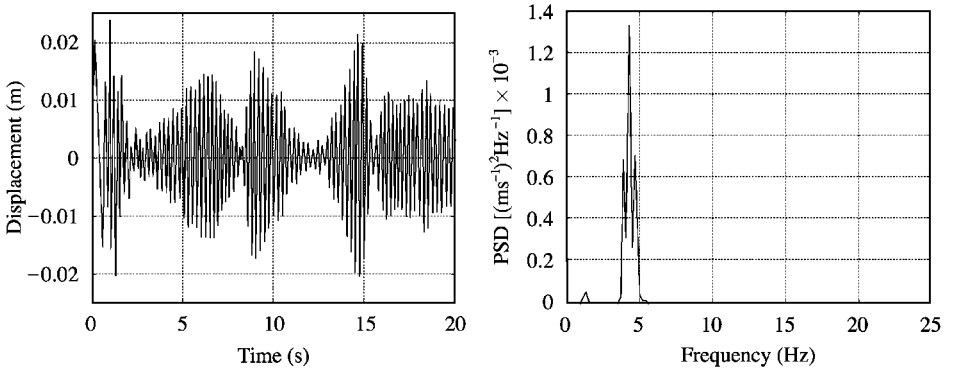

Figure 2. Time series of computed relative displacements (left panel) at $\xi = 0{\cdot}5$ togeter with its power spectral density (right panel) corresponding to rotating rig case 5004.

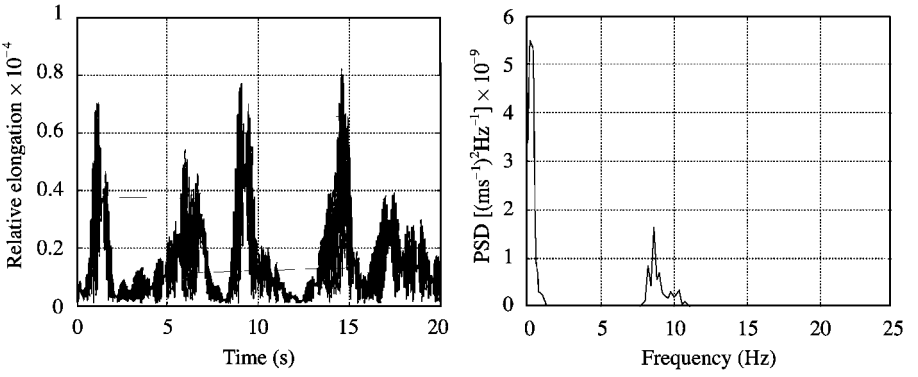

Figure 3. Computed time series of relative elongation (left panel) together with its power spectral density (right panel) corresponding to rotating rig case 5004.

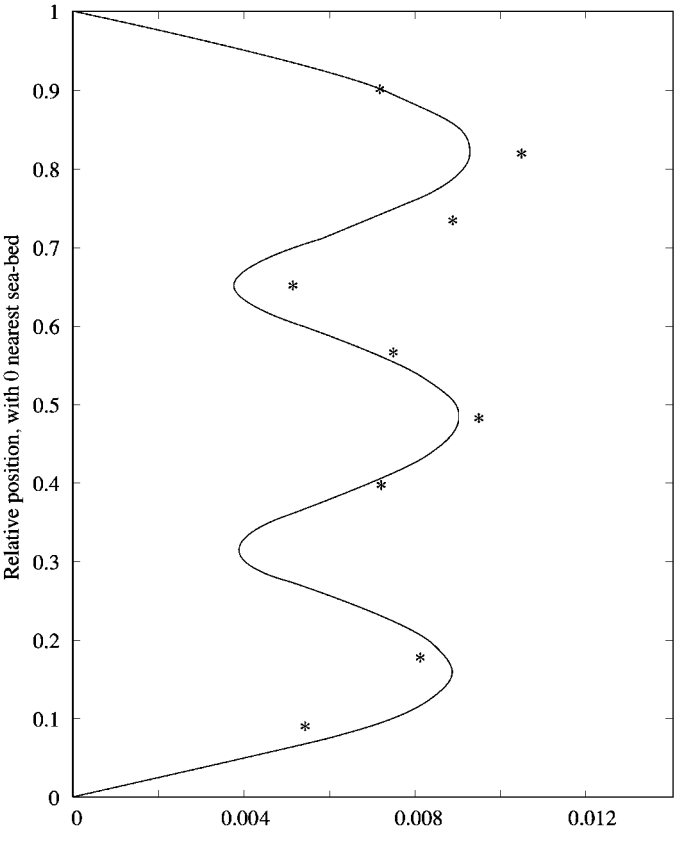

Figure 4. Comparison of STD of relative displacement (y/D) between rotating rig data (5104), shown as asterisks, and present model.

from the corresponding rig experiment. According to Figure 4, the transverse motion is dominated by the third mode. This is in good agreement with the observations. It is also apparent from Figure 4 that the model is able to resolve the main variability of the observed VIV motions.

The observed peak frequency was found to be nearly constant with depth and had a value of 3·8 Hz. This feature was also apparent in the simulations where the peak frequency was found to be 3·9 Hz.

The conclusion that can be drawn from these comparisons thus far, is that the model described in the foregoing is capable of reproducing the main features of the measurements, such as peak frequency and dominant modes, as well as the main variability of the displacements.

7. VALIDATION AGAINST "HANØYTANGEN" DATA

A series of model tests with deep-sea risers in a fjord at Hanøytangen has been carried out by Marintek (Huse 1997). One of the objectives was to provide experimental information on the performance of deep-sea risers regarding vortex-induced vibration in shear flow.

A riser with length of 90 m and diameter 0·03 m was instrumented for measuring bending moments in two directions at 29 different levels along the riser. The tests were done by suspending the riser from a surface vessel and towing it along a "floating quay" by moving the top end. For details, see Huse (1997). As for the rotating rig, this riser had also nearly neutral buoyancy, which justifies the approximation with uniform tension in the axial direction.

The simulation model was now set up for a test-case of linearly varying currents, ranging from of 0·56 m/s at the top point, to approximately 0·0 m/s at the sea-bed end (Huse 1997, test T13). The pretensioning for this specific test was $T = -1823$ N. As in the previous calculations, the drag coefficient was taken as constant at all depths and given by $C_0^{(k)} = 0$ and $C_1^{(k)} = 1{\cdot}2$. Damping and added mass coefficients and the density of sea water are $R = 1{\cdot}1\ \mathrm{kg}^{-1}\,\mathrm{ms}^{-1}$, $C_a = 1{\cdot}0$ and $\rho = 1025\ \mathrm{kg/m}^3$, respectively.

The model was, as in the previous case, started from a state of rest at time $t = 0$ by imposing a sudden hydrodynamic force given by equation (24) and with the same current profile as used in the test. Equation (9) was then integrated forward in time using a time step of $\Delta T = 0{\cdot}05$ s. The Strouhal number was prescribed at 10 spatial intervals by arbitrarily alternating its value between 0·19 and 0·20 from one layer to the next.

A closer examination of the observed time series together with model simulations, revealed that the number of excited modes in test T13 was above the limit which could be resolved with the given number of bending moment gauges. Hence, it was not possible to integrate the bending moments to displacements using direct methods. The comparison exercise is therefore carried out on the bending moments.

Figure 5 presents STD of the bending moments normal to the flow direction, as recovered from measurements (asterisk), Shear7 (dashed line) and the present model. The STD of the measurements are taken over a 33·3 s sequence of the time series (2001–6000) and should give a measure of the cross-flow vortex-induced vibration activity. The STD of the model time series was computed from the first 2000 iterations (100 s) using 90 eigenfunctions.

According to Figure 5, the Shear7 model predicts the 19th mode as the dominant one, while the present model gives the 13th. With 29 gauges (minus 5 that did not function), this indicates a possible lack of resolution in performing a direct integration of the measured bending moments to obtain displacements. This was also confirmed by a second-order integration algorithm which gave displacements due to VIV, far beyond the expected magnitudes of VIV.

A further comparison of the two models (Figure 5) indicates that Shear7 is producing larger amplitudes than the present model, except for the vicinity of the end-points, but the depth mean value is less. The mean deviation between model and observed data is slightly smaller for the present model than for Shear7.

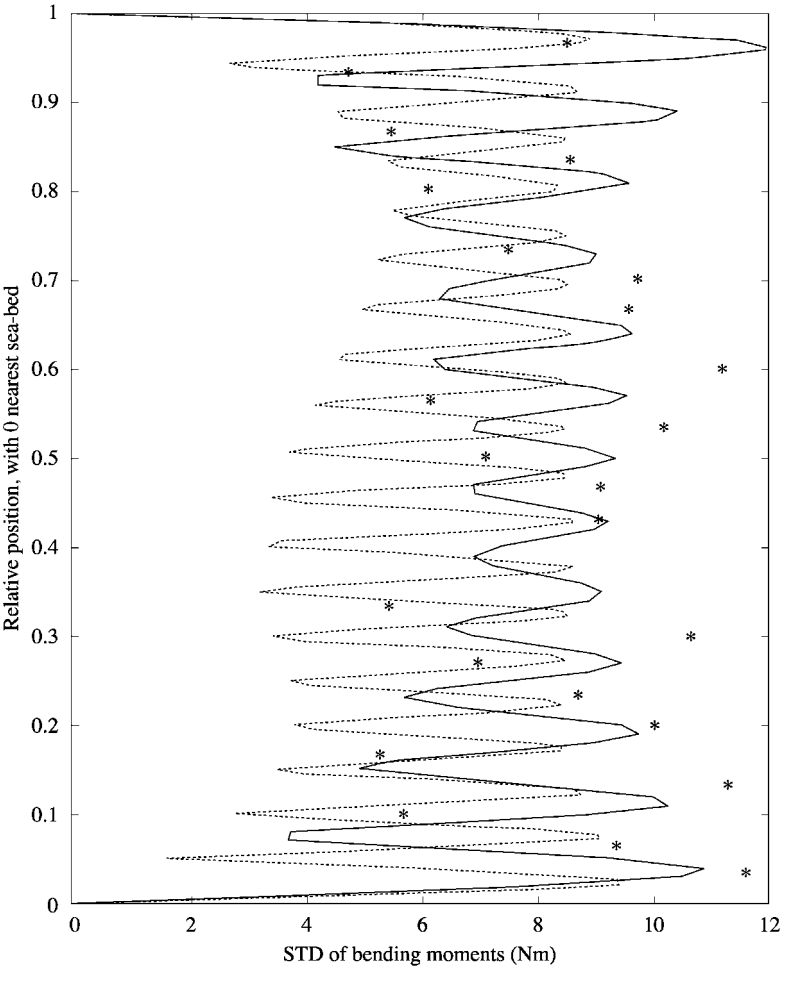

Figure 5. Standard deviation of the bending moments normal to the flow computed from present model, Shear7 and from Hanøytangen test-case T13: ----, Shear 7; *, measured; —, present model.

Time series, produced by the model, of displacements near $\xi = 0{\cdot}5$ and of the relative elongation are plotted in Figure 6. The PSD diagrams of the time series are plotted in the same figures.

Referring to Figure 6, it is seen that the amplitude of the displacement is varying with time. The variation is within one riser diameter, except at the beginning of the time series, where the sudden onset of the forcing leads to excitation of a transient first mode displacement. The two dominating frequencies of the displacements are at approximately 2·2 and 0·08 Hz. Regarding the elongation, the dominating frequencies are exactly twice these frequencies, namely 4·4 and 0·16 Hz.

For comparison purposes it is of interest to get an impression of how stable the observed frequencies are over time. The time series of test T13 were split into shorter sequences that were analysed separately. Taking the PSD of each sequence, it was found that the frequency distribution to some extent varied with time. However, significantly increased responses were generally observed around 2·3 Hz, which is close to the leading frequency found in the model simulation.

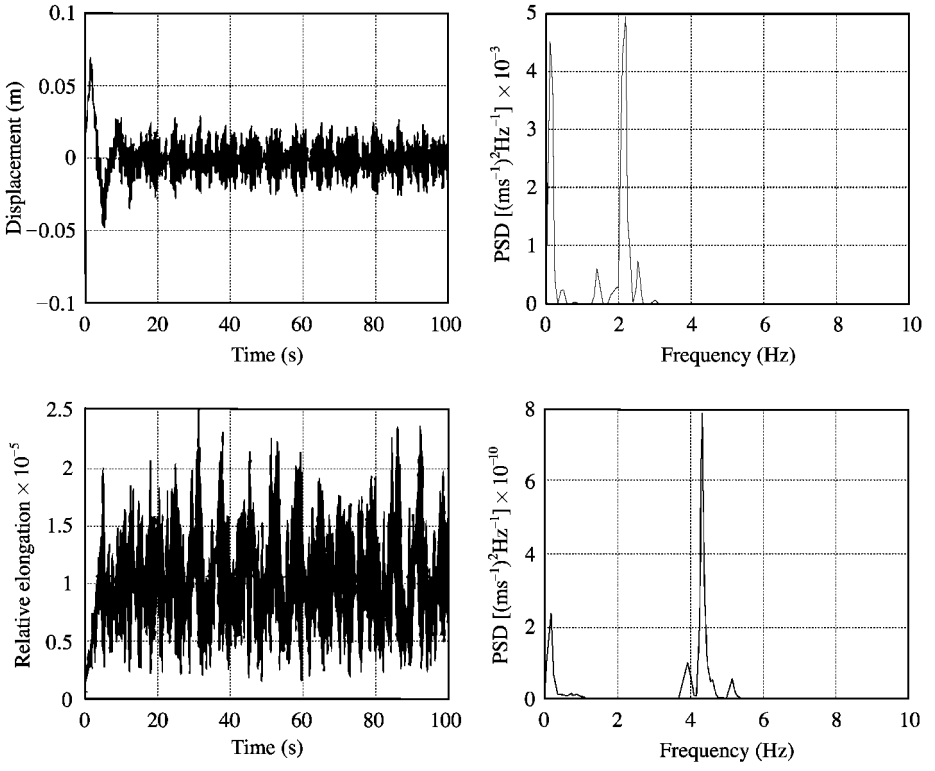

Figure 6. Computed time series of relative displacements (upper left panel) together with its power spectral density (upper right panel) and relative elongation (lower left panel) together with its power spectral density (lower right panel), corresponding to Hanøytangen T13.

In a subsequent test-case (T48) the tension was increased to $T = -3716$ N and the current velocity varied linearly from 0·95 m/s at the top point to near 0·0 m/s at the sea bed. The other parameters were as in test-case T13.

Figure 7 shows STD of the measured bending moments normal to the flow direction (asterisks) together with the corresponding model calculation, using the same parameter settings as for the T13 calculation (except pretensioning and current speed).

It is apparent from Figure 7 that, according to the model simulation, the 15–17th modes are excited along the riser. The amplitudes vary with depth and are most pronounced around the mid-point of the riser. The mean value of the bending moments is slightly higher above the mid-point than below, which is in accordance with the measurements. Similarly to the previous case, the depth mean value computed from the model is slightly lower than the observed value, which indicates that the chosen drag coefficient could be adjusted to achieve better agreement with measurements.

8. RESPONSE TO IMPULSIVE LOADS

Impulsive or shock loads are of great importance in the design of marine risers, where impacts from neighbouring risers, for example, may occur. This section deals with the conservation and distribution of energy when an impulsive force is imposed at a limited segment, denoted by l, of the riser. The segment is prescribed as symmetrical with respect to the mid-point of the riser, but any distribution may be chosen.

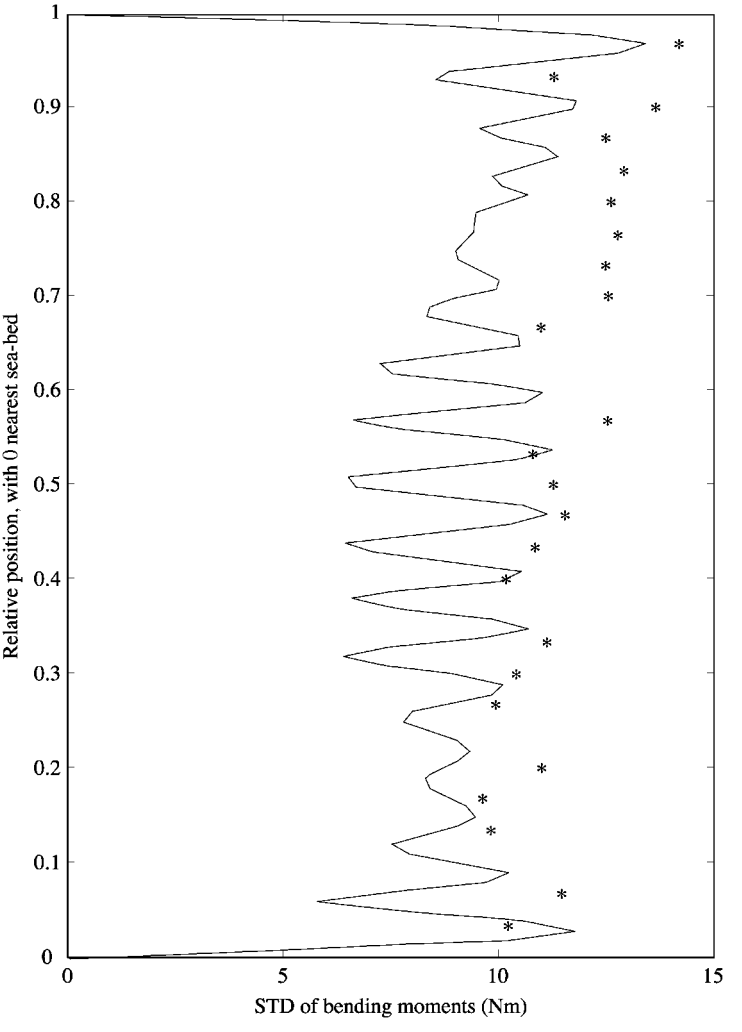

Figure 7. Standard deviation of the bending moments normal to the flow computed from present model and from the Hanøytangen test case T48 (asterisks).

The test-case T48 was set up to simulate the Hanoytangen riser using a pretensioning $T = -3716$ N. A sudden force of 500 N was imposed at time $t = 0$ with a duration of $\Delta t = 0{\cdot}1$ s. The force was prescribed to be constant along the entire segment which had the length $l = 0{\cdot}72$ m. The work exerted by the applied force can be computed from

$$W = Fl\bar{y}, \tag{27}$$

where F is the constant force and $\bar{y}$ is the mean displacement of the segment at the time Δt. By choosing $R = 0$ there is no energy dissipation in the system and the external work should be balanced by the sum of kinetic and potential energies, provided that no loss is introduced by the computational methods. The kinetic energy is expressed by

$$E_k = \frac{mL}{2} \int_0^1 \left(\frac{\partial y}{\partial t}\right)^2 \mathrm{d}\xi. \tag{28}$$

The potential energy consists of contributions due to axial tensions E_T and the bending strains E_S and can be expressed by

$$E_T = -T(S - L), \tag{29}$$

$$E_S = \frac{EI}{2L^3} \int_0^1 \left(\frac{\partial^2 y}{\partial \xi^2} \right)^2 \mathrm{d}\xi. \tag{30}$$

In equation (29), $S - L$ is the riser elongation. The kinetic and potental energies are now easy to evaluate using the expressions for y and S given above.

Figure 8 presents time series of E_k, E_T and E_S using 90 eigenfunctions. It is seen from Figure 8 that the potential energy is dominated by the variation of the axial tension. The

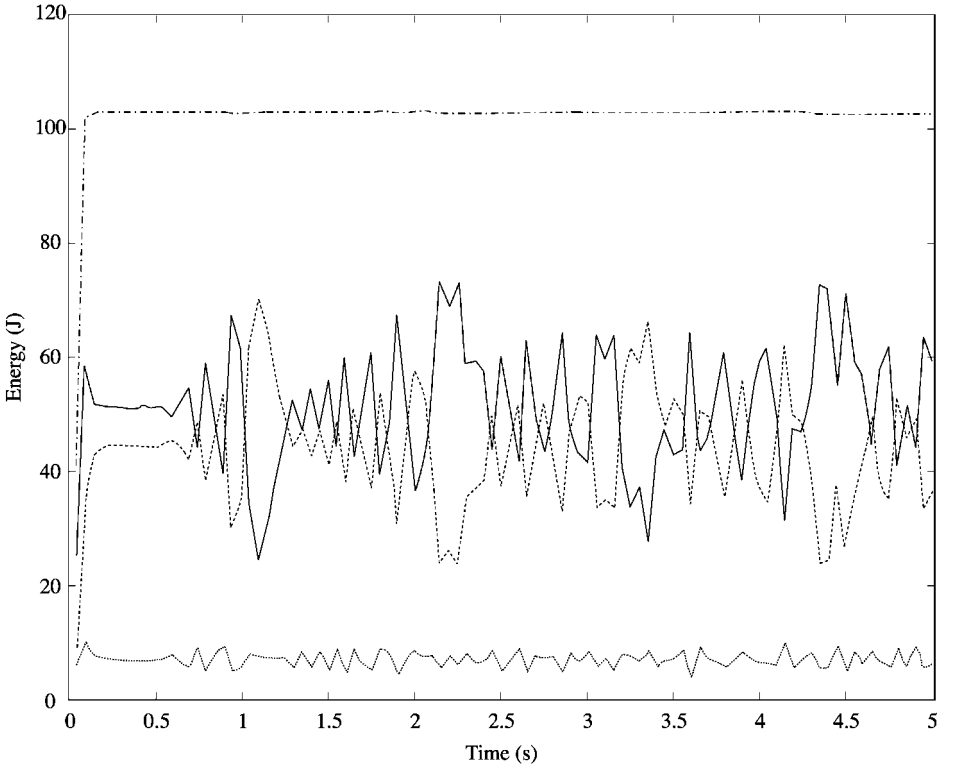

Figure 8. Time series of energy due to an impulsive forcing. Kinetic energy is denoted by E_k, potential energy components by E_T and E_S, and the total energy by V:—, E_k; - - -, E_T; . . ., E_s; -·-·-. V.

TABLE 1

Total response energy computed using an increasing number of eigenfunctions M; imposed energy: 102·83 J

$M = 20$	$M = 40$	$M = 60$	$M = 90$
$V = 93{\cdot}42$ J	$V = 101{\cdot}42$ J	$V = 102{\cdot}40$ J	$V = 102{\cdot}77$ J

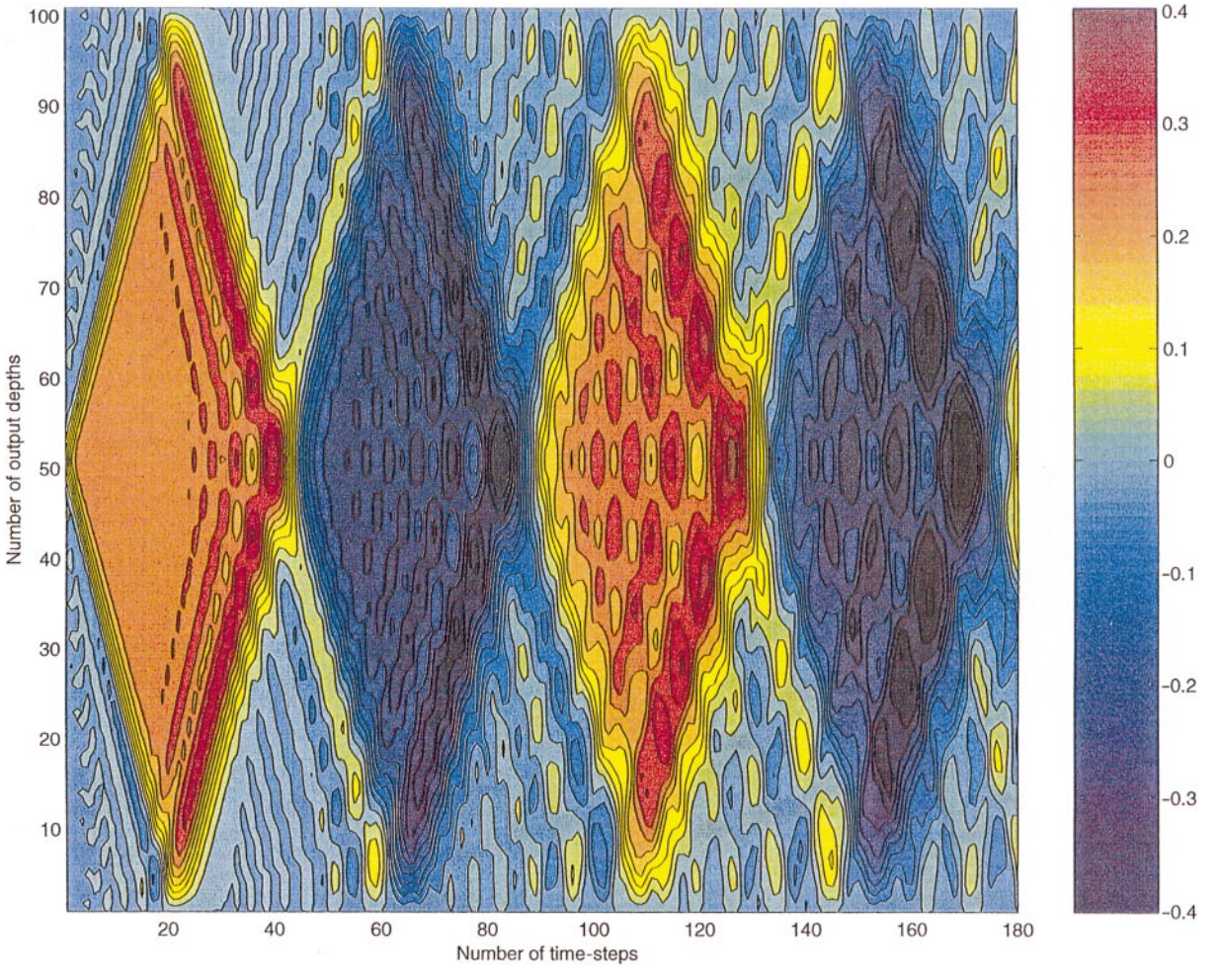

Figure 9. Contours of displacement versus time due to an impulsive force.

total energy

$$V = E_k + E_T + E_S$$

is also presented in the figure. It is evident that the total energy is nearly constant after the impact phase. A long-term simulation with the same set-up confirms that the energy is conserved in the model.

From equation (27) it was found that the work due to the external forcing is 102·83 J. The Table 1 presents the total energy V computed for different number of eigenfunctions M. It is evident from the table that, as the number of functions is increased, the total riser energy approaches the work exerted by the external force. Using 90 eigenfunctions, the total energy is 102·77 J or above 99·9% of the applied external energy.

The energy caused by the impulsive forcing is transported away from the impact area in the form of waves. As the forcing is completely symmetrical with respect to the midpoint of the riser, equal amounts of energy are transported towards the end-points, where they are then reflected. This is demonstrated in Figure 9 where contours of displacement versus time are plotted. The symmetrical distribution is evident from this figure.

9. CONCLUDING REMARKS

A model has been formulated to examine riser displacements due to time- and depth-dependent currents. The model has been applied to two physical test-cases that have been carried out to study vortex-induced vibrations. Comparisons between simulated and measured transverse displacements and bending moments revealed a good correspondence between modelled and measured data.

The model reponse to a prescribed external impulsive force has also been examined. By comparing the external work on the riser with the total response energy (kinetic plus potential), it turns out that the model accurately conserves energy. Long-term simulations with the model did also confirm that there is no artificial energy dissipation using the method described in this paper.

There is a wide range of values for the drag/lift and damping coefficients in the literature. The values chosen in this paper were more or less arbitrarily selected within this range. Model comparisons versus the Hanøytangen data indicate a consistent deviation that most likely could be reduced by a "tuning" of the coefficients.

The model formulation was worked out for a constant axial pretensioning T. However, it is easy to reformulate the model to include a prescribed axial variation of the pretensioning.

ACKNOWLEDGEMENTS

The author wishes to thank Norsk Hydro, Exxon Production Research Company, Amoco Production Company, Mobil Business Resources Corporation, ARCO Exploration and Production Technology, BP Exploration Operating Company and STATOIL for permission to use the Rotating Rig data in the present study and to Dr Len Gray for valuable comments. I am also indebted to my collegues Gudmund Kleiven and Gudmund P. Olsen for their contribution during the progress of this work.

References

Halse, K. H. 1997 On vortex shedding and prediction of vortex-induced vibrations of circular cylinders. Dr. Ing Thesis, Department of Marine Structure, Faculty of Marine Technology, NTNU/Trondheim, Norway.

HUSE, E. 1997 Large scale testing of riser models, main report. Report no. 513106.00.01 Norwegian Marine Technological Institute, Trondheim, Norway.

KING, R. 1977 A review of vortex shedding research and its application. *Ocean Engineering* **4,** 141–171.

MO, K. & H. LIE 1997 Model tests of a staggered buoyancy riser in a rotating rig. Report no. 513105.00.02 Norwegian Marine Technological Institute, Trondheim, Norway.

NEWMAN, D. & G. E. KARNIADAKIS 1997 A direct numerical simulation study of flow past a freely vibrating cable. *Journal of Fluid Mechanics* **344,** 95–136.

VANDIVER, J. K. & L. LI 1994 SHEAR7 Program Theoretical Manual. Department of Ocean Engineering, MIT, Cambridge, MA, U.S.A.